4288 *Macromolecules* **2009**, *42*, 4288–4299
DOI: 10.1021/ma8027547

Macromolecules
ARTICLE

Formation of Ca^{2+}-Induced Intermediate Necklace Structures of Polyacrylate Chains

Sebastian Lages,[†] Peter Lindner,[‡] Prashant Sinha,[§] Anton Kiriy,[§] Manfred Stamm,[§] and Klaus Huber*,[†]

[†]*Chemsitry Department, Universitat Paderborn, Warburger Strasse 100, D-33098 Paderborn, Germany,* [‡]*Institute Laue-Langevin, LSS Group, B.P. 156, 6, rue Jules Horowitz, F-38042, Grenoble, Cedex 9, France, and* [§]*Leibniz-Institut für Polymerforschung Dresden e.V., Hohe Strasse 6, 01069 Dresden, Germany*

Received December 10, 2008; Revised Manuscript Received April 28, 2009

ABSTRACT: Long chain sodium polyacrylate polymers in dilute aqueous solution respond extremely sensitive to the addition of small, stoichiometric amounts of Ca^{2+} ions. Essential features of this response are a considerable shrinking of the coil dimensions and an additional sensitivity of the coil dimensions toward a change in temperature. To reveal details of this shrinking process, the conformational changes in response to the addition of alkaline earth cations at two different temperatures are investigated by means of light and neutron scattering and by AFM on the same samples, respectively. Partially collapsed coils at 15 °C were further shrunken and modified in shape by increasing the temperature to 30 °C. The scattering curves from the intermediates at 30 °C could successfully be interpreted with a pearl necklace model, which includes a low amount of pearls per polymer separated by 80 nm from each other. AFM investigations of adsorbed chains confirm the drastic conformational changes inferred to the system with the temperature increase by 15 °C. The results are considered to be one of the rare direct evidence for a pearl-necklace-like intermediate along the coil-to-globule transition of polyelectrolyte chains.

Introduction

The shrinking of polymer coils in poor solvents is a mature topic in polymer science, yet it has not lost any of its attractiveness. Originally driven by a purely fundamental interest in the coil-to-globule transition postulated by Stockmayer[1] and de Gennes,[2] it has meanwhile gained a considerable technological relevance. This relevance is due to the fact that the process has model character for potential applicabilities in responsive materials.

The collapse of coils to compact spheres has been proven for the first time in 1980 by Sun et al.[3] Successively, several features of intermediate structures have been addressed. Chu et al.[4] identified a two stage process with the first stage being attributed to a nucleation and growth of beads along the chains, which further grow and merge during a second stage. A considerable experimental hurdle to be overcome was the speed of these structural changes. At the same time Kuznetsov et al. presented Monte Carlo simulations for the kinetics of the coil-to-globule transition where locally collapsed domains along the coils are formed initially which in a second stage grow in size and eventually combine to form a single sphere within a chain.[5] This schematic is emphasized because it may bear similarities to the subject of the present report.

Theoretical postulations concerning a similar transition of polyelectrolytes have been first presented by Kantor and Kadar[6] and Rubinstein et al.[7] who transferred the concept of the shape instability of charged oil droplets to collapsing organic polyampholeytes and homogeneously charged polyelectrolyte coils in water respectively. Unlike the oil droplets, however, the resulting subdroplets of partially collapsed charged polyelectrolyte coils remain interconnected by string-like coil segments. The reversed expansion of such collapsed polyelectrolytes leads to a cascade of transition states, which resemble necklace-like structures. These transition states bear only partial similarity to the electrically neutral intermediates[5] mentioned above. Contrary to the latter, the electrostatics of polyelectrolyte intermediates aligns the splitting beads equidistantly along a straight line if no additional salt is present in solution. This structure shall be denoted as stretched pearl necklace chain in the present article. Screening of electrostatic repulsions due to an added salt may disturb this alignment of beads. It is also worth being noted that the electrostatic nature of the shrinking coils may stabilize intermediates and thus makes its investigation easier than in the case of neutral polymers. As could be revealed by further theoretical investigations and simulations, a subtle interplay of solvent quality for the hydrophobic backbone, of polymer concentration and of the degree of electrical charging is required to generate such necklace-like intermediates.[8−11] In the necklace regime, a large fluctuation of the bead size and number of beads per chain occurs within a sample.[9−11]

If all other parameters are appropriately fixed, coil shrinking can be induced by its discharge. Discharge of a polyelectrolyte is achieved either by counterion condensation, by complex bonding of specifically interacting counterions, by variation of the fraction of chargeable groups in a copolymer or by changing the solvent quality for the polymer. A survey of these contributions is given recently.[12] Discharging polyelectrolyte coils with specifically interacting cations—usually protons or multivalent metal cations—is especially appealing for two reasons: (i) it avoids a cosolvent, and (ii) it has a stronger impact than counterion condensation. Yet, as we will see, specifically interacting counterions in the presence of an additional inert salt modify the formation of stretched necklace chains, anticipated theoretically[7−11] in salt-free solution.

*To whom correspondence should be addressed. E-mail: klaus.huber@uni-paderborn.de. Telephone: (49) 5251602125. Fax: (49) 5251604208.

 Published on Web 05/19/2009

Many of the experimental reports on polyelectrolyte shrinking support the model of a necklace-like chain conformation. However it is the number of indications rather than a clear-cut proof, which seems to confirm the theoretical predictions. Experiments which are considered to reveal the most direct indications for pearl necklace structures are small angle scattering curves from single chains and atomic force microscopy (AFM) images of isolated coils.

Geissler et al.[13] induced the shrinking of polyelectrolytes in salt-free water by addition of acetone and performed small angle neutron scattering (SANS) experiments with collapsed chains. By comparing the overall size of polyelectrolyte chains with the behavior of the scattering curves at high q-values, they found an indication for a string of three to four beads. Schweins et al.[14] investigated the collapse of NaPA, induced by divalent alkaline earth cations. Only in one case did the trend of a combined light and small angle neutron scattering provide data of sufficient quality in the q-regime appropriate to provide clear evidence for a bead−bead correlation as a characteristic feature of necklace chains. More recently, Boué et al.[15] succeeded in revealing indications for necklace structures in semidilute solution of partially sulfonated polystyrene sulfonate. Form factors of single chains could be extracted by means of the zero average contrast method and depending on the degree of sulfonation yielded contributions from elongated chain segments and spherical entities.

Contrary to scattering techniques, microscopy provides images in real space, yet with the disadvantage that chains can only be imaged after the adsorption process thus putting considerable strain on the polymer coils while preparing the samples. Recently AFM has been successfully used for the study of the coil shrinking of relatively large synthetic polyelectrolytes. Stamm et al.[16,17] induced this shrinking for poly(2-vinylpyridine) and poly(methacryloyloxyethyl dimethylbenzylammonium chloride) by addition of Na_3PO_4 as a low molecular weight salt, which screens intermolecular repulsions. They succeeded to image a cascade of transition states with necklace shape on mica substrates. The number of beads and the length of the interconnecting strings decreases, while the size of the beads increases with increasing salt concentration in the preceding solution state. In a closely related experiment, Borkovec et al.[18] observed essentially the same trend with poly(vinylamine). In the latter experiment a direct discharge of the respective poly (vinylammonium) salt was achieved by decreasing the pH. Noteworthy, all captured necklace-like structures are closer to an arrangement of beads along a semiflexible chain than to an equidistant placement of beads along a straight line (stretched necklace).

AFM makes accessible the conformation of *adsorbed* polyelectrolyte coils. During adsorption, the conformation of long polymers is inevitably modified by the transition from three to two dimensions (2D).[19] Loss of one degree of freedom drastically reduces the number of possible configurations that the molecule can access within the range of the thermal energy. In principle, three distinct cases of molecule-surface interactions can be postulated: (1) the molecules freely equilibrate on the surface as in a 2D solution before they are captured in a particular conformation, (2) the polyelectrolyte coils adsorb irreversibly whereby the interaction with substrate changes the polymer conformation, leading to their partial local spreading, or (3) the molecules adhere to the substrate without being equilibrated, and the resulting conformation resembles a projection of the actual 3D conformation onto the surface. The latter scenario corresponds to kinetic trapping of the molecules onto the surface. In the light of these three distinct cases, it is fully justified to ask how much the conformation of adsorbed molecules reflects the respective conformation in solution before adsorption.

The aim of the present contribution is to shed further light on the shrinking of the dimensions of polyelectrolytes which follow a coil-to-globule transition. The system under consideration is sodium polyacrylate (NaPA) in dilute aqueous solution in the presence of 0.01 M NaCl as an inert electrolyte. NaPA precipitates upon addition of stoicheometric amounts of Ca^{2+} or other alkaline earth cations. While approaching this precipitation threshold by variation of either component concentration, the PA coils shrink and collapse to compact spheres.[12,20] In the present work, the shrinking process is induced by an exchange of a small fraction of the Na^+ ions in solution by Ca^{2+} ions whereby the overall concentration of cationic charges was kept constant. This procedure has been proven to be extremely successful in a series of preceding investigations.[12,14,20] In addition to the variation of the Ca^{2+} concentration, the temperature has been introduced as a second parameter to approach the collapse threshold. The latter impact is based on the fact that the complex formation of the COO^- residues with Ca^{2+} ions is entropic in nature.[21,22] As a consequence, Ca^{2+} induced coil shrinking and intermolecular precipitation of CaPA at a constant Ca^{2+} content is enhanced by a temperature increase. All experiments are carried out with a NaPA sample, which has a weight averaged molar mass of 783 kDa.

In order to reproduce our earlier findings on the CaPA system,[14] where direct indications of necklace like intermediates has in fact been collected just for one specific CaPA sample by SANS, we performed an additional set of combined experiments. Beyond it, these experiments are designed to give a definite answer to the following question: Is it possible to confirm the necklace shape for single NaPA coils in dilute solution which undergo a coil-to-globule transition upon discharge with specifically interacting counterions? AFM can supplement scattering experiments in an almost ideal way and is superior to any scattering experiment as it presents a direct view of adsorbed polymer coils. Yet, its disadvantage is a largely uncontrollable relaxation and strain on the coils during the sample preparation, i.e. during adsorption on a surface. With these aspects in mind, the same samples used for SANS above shall be subdued to AFM experiments. As a result we will be able to add information to a second question: Do AFM images on shrinking polyelectrolyte coils succeed to reveal the essential features which the very coils exhibit in dilute solution respectively and therefore provide a reliable tool to investigate dilute solution behavior of polyelectrolyte coils? If the answer is yes, we can additionaly confirm and image in direct space the shape of shrinking intermediates, observed by SANS.

Experimental Section for Scattering Experiments and Sample Preparation

Materials. The sodium polyacrylate was purchased from Polysciences (Eppelheim, Germany). NaCl, dry $CaCl_2$ and NaOD (40% w/w in D_2O) were of analytical grade from Fluka (Buchs, Switzerland), and Sigma-Aldrich (Taufkirchen, Germany). D_2O was purchased from Deutero GmbH (Kastellaun, Germany) and was used without further purification. Prior to light scattering experiments all solutions were purified from dust by filtration with filters from Millipore (Eschborn, Germany). For solvents and solutions 0.22 μm CA filters and 0.45 μm PVDF filters were used, respectively. A sodium polyacrylate sample, denoted as P804, was used in all experiments. P804 was analyzed in 0.01 M aqueous NaCl at a pH of 9 by means of combined static (SLS) and dynamic (DLS) light scattering at 25 °C. A stock solution with a NaPA concentration of c = 0.1584 g/L was used as a basis for a Zimm/Berry analysis[23] for a dilution series. The results of the characterization are summarized in Table 1.

Selection of Samples for SANS. SANS experiments were performed to investigate coil shrinking in dilute solutions of

Table 1. Results of the Characterization of Sample P804 in 0.01 M NaCl and the Light Scattering Analysis of SASE Performed before and after the SANS Experiments and of SASH Performed after the SANS Experiments

sample	T/°C	M_W/(g/mol)	R_g/nm	R_h/nm
P804	25	783 000 ± 13 500	125.8 ± 4.1	76.8 ± 2.0
SASE before SANS	15	1 140 000 ± 13 700	34.3 ± 0.9	31.2 ± 0.3
SASE after SANS	15	935 000 ± 11 200	38.3 ± 0.8	31.3 ± 0.4
SASE before SANS	30	978 000 ± 8800	19.3 ± 1.1	15.8 ± 0.1
SASE after SANS	30	1 010 000 ± 11 100	25.6 ± 1.0	15.4 ± 0.3
SASH	15	1 090 000 ± 22 900	52.8 ± 1.1	40.0 ± 0.9
SASH	30	1 190 000 ± 26 200	32.8 ± 1.6	15.7 ± 0.3

NaPA in the presence of Ca^{2+} ions in the vicinity of the Ca^{2+}/NaPA phase boundaries at 15 and 30 °C. This requires appropriate solutions where the CaPA coils exhibit a considerable degree of shrinking. The degree of shrinking preferably has not yet reached the sphere limit. Selection of appropriate solutions was based on a combinded SLS and DLS analysis. For this purpose, three different stock solutions were prepared: (i) A solution of 0.01 M NaCl in D_2O was set to pH = 9 using 0.01 M NaOD in D_2O; (ii) the NaPA was dissolved in D_2O containing 0.01 M NaCl whereby the resulting solution was gently mixed for three days; (iii) additionally, a solution of dry $CaCl_2$ and NaCl was prepared in D_2O at a pH = 9 set with 0.01 M NaOD. By combining appropriate amounts of the three stock solutions, samples with different $[Ca^{2+}]$/[PA] ratios were prepared whereby the concentration of cationic charges [C] in this solutions was $[C] = [Na^+] + 2[Ca^{2+}] = 0.01$ M.

The samples were successively analyzed by means of combined DLS and SLS. Light scattering experiments were carried out using a model 5000E CGS from ALV-Laser Vertriebsgesellschaft (Langen, Germany), equipped with a Nd:YAG laser with 200 mW operating at a wavelength of 532 nm. Cylindrical quartz glass cells with an outer diameter of 20 mm from Hellma (Müllheim, Germany) served as cuvettes for light scattering experiments. Light scattering experiments were performed at 15 and 30 °C. The temperature was set to the desired values with a precision of 0.01 °C using a C25 Haake bath. The scattering intensities were recorded in an angular regime of $30° \leq \theta \leq 150°$. Extrapolation to zero concentration was not sensible because different $[Ca^{2+}]$/[PA] ratios lead to different coil sizes. Hence, SLS and DLS experiments were analyzed by solely extrapolating scattering data to zero scattering angle according to eqs 1 and 2, respectively,

$$\frac{Kc}{\Delta R_\theta} \cong \frac{1}{M_w} + \frac{R_g^2 q^2}{3M_w} \quad (1)$$

$$D \cong D_z(1 + CR_g^2 q^2) \quad (2)$$

In eqs 1 and 2, M_w, R_g^2, and D_z are the weight averaged molar mass, the *z*-averaged mean square radius of gyration and the z-averaged diffusion coefficient, respectively. By means of the Stokes−Einstein equation, the diffusion coefficient can be transformed into a hydrodynamically effective radius R_h

$$R_h = \frac{k_B T}{6\pi\eta D_z} \quad (3)$$

with T the absolute temperature in Kelvin, k_B the Boltzmann constant, and η the solvent viscosity. Temperature dependent viscosity and refractive index data were interpolated using eqs 11 and 12 of ref 22. A refractive index increment of $(\partial n/\partial c) = 0.1709$ mL/g for NaPA in 0.01 M NaCl was used in all LS experiments.[23]

Two samples have been selected as suitable for SANS experiments. NaPA and Ca^{2+} concentration in the sample denoted as SASE were $c = 0.2346$ g/L of NaPA (2.50 mM) and $[Ca^{2+}] = 1.00$ mM respectively. The second sample, denoted as SASH, contained 0.13 g/L of NaPA (1.38 mM) and 0.65 mM Ca^{2+} ions. The coil dimensions are drastically decreased compared with the dimensions of NaPA in 0.01 M NaCl without Ca^{2+} ions (cf. Table 1 and Figure 1). The extent of shrinking is more pronounced at 30 °C. Analysis was performed at 15 and 30 °C by means of combined DLS and SLS. All data were evaluated in an angular regime $60° \leq \theta \leq 150°$, corresponding to a q-regime of $0.015\ nm^{-1} \leq q \leq 0.03\ nm^{-1}$. The first three data points have been always omitted for this analysis because they occasionally exhibited a strong fluctuation of the scattering signal, probably caused by the formation of aggregates. Further justification for this procedure of data analysis is provided in the Supporting Information and by the proof of sample stability.

Proof of Sample Stability. The samples selected for SANS were solutions of NaPA coils which exhibited a pronounced extent of coil shrinking and were located close to the phase boundary.[20,22] This requires a proof of the stability for a time period which includes sample preparation, sample transfer to the ILL site and the SANS experiment. To this end, SASE as one of the selected samples was analyzed prior to the transfer of the samples to the ILL and after SANS. After the SANS experiment, we prepared a solution from sample SASE from the same stock used already for the analysis prior to the SANS experiments. The resulting shelf life was 12 days. Analysis was performed at 15 and 30 °C by means of combined DLS and SLS. All data were evaluated in an angular regime $60° \leq \theta \leq 150°$, corresponding to a q-regime of $0.015\ nm^{-1} \leq q \leq 0.03\ nm^{-1}$. The resulting scattering curves are shown in Figure 2. As already mentioned, the lowest scattering angles occasionally exhibited excess scattering intensity. Once such an excess occurred, it decreased or disappeared during the shelf life. At $q \geq 0.015\ nm^{-1}$ the scattering curves remained essentially unaltered. This clearly indicates stability of sample SASE and therefore comfirms that SANS experiments could be performed with the same single coils as observed with the preparatory DLS/SLS analysis prior to SANS. The results of the temperature dependent DLS/SLS experiments and of the stability tests are summarized in Table 1.

SANS Experiments. SANS experiments were carried out on the small angle neutron scattering instrument D11 at the Institut Laue-Langevin (ILL, Grenoble, France). The samples were put into a sample changer rack. The temperature was controlled by using a Haake bath with a precision of 0.1 °C. The actual temperature in the rack was measured online by putting a Pt100 in a water-filled cell. For solvents and solutions, Hellma cells with a path length of 5 mm were used. Water (H_2O) in a sample container with a path length of 1 mm was applied as calibration standard. SANS investigations were performed on both samples, SASE and SASH, at 15 and 30 °C at sample−detector distances of 1.10, 2.50, 10.00, and 22.00 m. Additionally, a measurement at 30 °C with SASE and the corresponding solvent was performed applying a sample−detector distance of 28.00 m. For all measurements a constant wavelength of 0.6 nm was used resulting in a range of momentum transfer of $0.02\ nm^{-1} \leq q \leq 3.3\ nm^{-1}$. Scattering intensities were recorded with a 2-dimensional position-sensitive ^3He detector consisting of 64×64 cells with a spatial resolution of 1 cm^2. Transmissions were determined by measuring the direct, attenuated beam (i.e., $q = 0$) passing through any object I_x which was divided

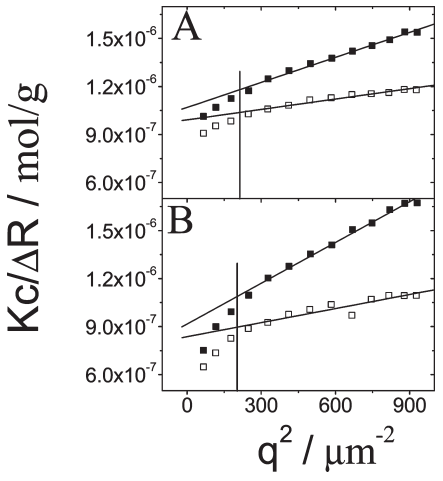

Figure 1. Results of static light scattering experiments for SASE (A) and SASH (B). The full symbols refer to the experiments at 15 °C whereas the open symbols refer to the data taken at 30 °C. The data points on the left of the vertical line were not considered for further data evaluation at both temperatures. All data were recorded after the SANS experiment.

by the respective measurement of the incident beam I_i. according to eq 4

$$T_x = \frac{I_x(q=0)}{I_i(q=0)} \tag{4}$$

The scattering data were treated using the ILL standard software package.[24] The 2-dimensional raw data were radially averaged after location of the central detector coordinates for each sample−detector distance. Normalization of the scattering intensities was achieved via the calibration standard H_2O. The wavelength dependent effective differential cross-section $(d\Sigma/d\Omega)_{H_2O} = 0.905\ cm^{-1}$ of H_2O for the ^3He detector (at a wavelength of 0.6 nm) is taken from ref 25. The differential scattering cross-section of a solution is obtained by direct subtraction of the corresponding solvent according to eq 5

$$\left(\frac{d\Sigma}{d\Omega}\right)_S = \left(\frac{(I_S - I_{Cd}) - \frac{T_S(1-n_S\tau)}{T_{SOLV}(1-n_{SOLV}\tau)}(I_{SOLV} - I_{Cd})}{(I_{H_2O} - I_{Cd}) - \frac{T_{H_2O}(1-n_{H_2O}\tau)}{T_{EC}(1-n_{EC}\tau)}(I_{EC} - I_{Cd})}\right) \times \left(\frac{T_{H_2O}(1-n_{H_2O}\tau) \times 0.1\left(\frac{d\Sigma}{d\Omega}\right)_{H_2O}}{T_{SOLV}(1-n_{SOLV}\tau) \times 0.5}\right) \tag{5}$$

The indices denote sample cell (S), solvent cell (SOLV), standard (H_2O), empty cell (EC), and cadmium (Cd). The Cadmium measurement provides the electronic background. The term $(1 - n\tau)$ takes into account the correction for dead time losses with n being the integral count rate of each measurement and τ being the dead time. Sample background was appropriately considered by subtracting the scattering profile of the solvent cell from the polymer solution cell. This procedure saves separate subtraction of the empty cell from sample and solvent respectively and is highly recommended at low sample signal intensities. The incoherent contribution to the scattering intensity, which can be attributed to the presence of hydrogen in the polymer, was determined to be 2.7 $10^{-5}\ cm^{-1}$ and was thus subtracted from the scattering curves.

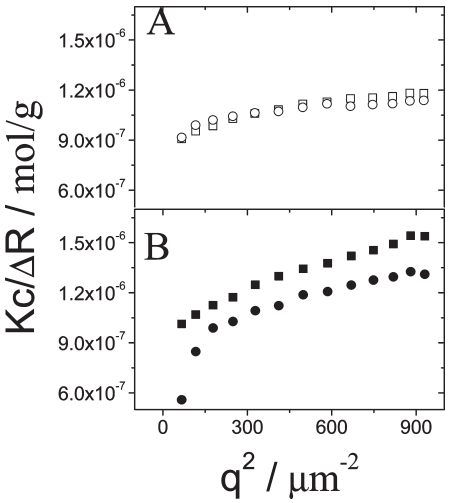

Figure 2. (A) Sample SASE at 30 °C: (○) LS experiments before SANS experiments; (□) LS experiments performed after SANS experiments. (B) Sample SASE at 15 °C: (●) LS experiments before SANS experiments; (■) LS experiments performed after SANS experiments;

Experimental Section for AFM Experiments

Materials. Dry lanthanum chloride was of analytical grade and purchased from Sigma-Aldrich (Taufkirchen, Germany). Chemical modification of mica surfaces was carried out using (3-aminopropyl)dimethylethoxysilane (97% purity) from ABCR GmbH (Karlsruhe, Germany). Toluene and sodium (>99% purity in terms of trace metals) were of analytical grade and purchased from Arcos Organics (New Jersey, USA) and Merck Schuchardt OHG (Hohenbrunn, Germany), respectively. PTFE filters (0.2 μm) were used to remove any dust particles in solutions and were purchased from Carl Roth GmbH (Karlsruhe, Germany). Temperature of the samples and substrates was set to desired values using a standard type E 200 water thermostat from Lauda-Dr. R. Wobser GmbH (Königshofen, Germany).

Sample Preparation. Freshly cleaved mica surface was chosen as the most appropriate substrate because its unique flatness allows single molecular resolution.[16−18,26] It is fairly well established that polyacrylates do not adsorb on pristine mica surfaces because of strong electrostatic repulsion forces acting at the substrate-sample interface.[27,28] Thus, kinetic trapping of such polyelectrolyte molecules on the surface can be affected only with the aid of suitable pretreatment agents capable of shielding this repulsion.

Following earlier works,[28−30] several pretreatments were applied. In our case, the best results were obtained when mica was pretreated with a solution of La^{3+} salt prior to the adsorption of polyacrylate. Freshly cleaved mica surfaces were treated with a solution of 0.01 g/L $LaCl_3$ in Millipore water for 1 min, which was successively removed with a flux of N_2. The substrates so prepared were fixed at the outer surface of a hollow aluminum tubelet, attached to a water bath which served as a thermostat. The thermostat was adjusted to the two desired temperatures, corresponding to 15 and 30 °C. The sample solutions SASE and SASH to be adsorbed were also equilibrated at the same temperatures respectively. After equilibration, a drop of sample solution was put on the substrate for 2−3 s and successively the solvent was removed with a flux of N_2. The substrate was then taken for AFM imaging. In addition, reference experiments were also performed at room temperature. In these reference experiments, denoted as REFE and REFH, the same concentration of NaPA and total salt were used as for SASE and SASH respectively, yet without $CaCl_2$.

In an alternative procedure, mica surfaces were pretreated with silanes. This procedure has also been cited to be an appropriate method for adsorbing charged polyelectrolytes on mica surfaces.[18,31,32] The silanes customarily used for such

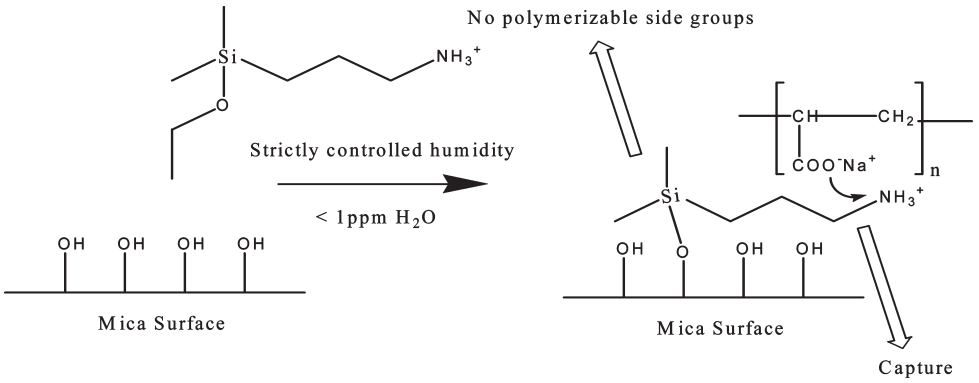

Figure 3. Schematic representation of chemical modification of mica surface using (3-aminopropyl)dimethylethoxysilane (APDMES).

chemical modifications have been both monofunctional like (3-glycidoxypropyl)dimethylethoxysilane[18] and multifunctional like (3-glycidoxypropyl)trimethoxysilane[18] or (3-aminopropyl) triethoxysilane.[31,32]

The quality of mica surfaces chemically modified with multifunctional silanes has been reported to be quite sensitive to ambient humidity.[32] Depending upon the exact chemical modification procedure followed, AFM scans of mica surfaces modified with multifunctional silanes have shown formation of large aggregates.[31] These aggregates are speculated to be condensation products resulting from the silanization process itself.[18] In the latter case, it becomes quite difficult to differentiate between condensation products formed on the surface of mica as a result of silanization and actual aggregates from the polyelectrolyte specie under investigation.[18] For our case, the thermal equilibration required for the chemically modified mica surface at a particular temperature prevented a strict control of humidity. Thus, a monofunctional aminosilane like (3-aminopropyl)dimethylethoxysilane (APDMES), having only one ethoxy group to bind the hydroxyl groups of the mica surface, was expected to greatly reduce the probability of side condensation reactions. Its amino head would capture the negatively charged polyelectrolyte as shown schematically in Figure 3. In fact, APDMES gave the best results and chemical modification was carried out using monofunctional APDMES in the present work.

An APDMES−toluene solution (0.01% V/V) was dropped on freshly cleaved mica and evaporated under glovebox conditions (oxygen < 1 ppm, water < 1 ppm). The surface was washed several times under laboratory hood conditions using dry (refluxed over Na) toluene filtered previously through a filter of pore size 200 nm. The remaining procedure was the same as in case of $LaCl_3$ pretreatment. Both samples, SASE and SASH, were thermally equilibrated at 15 and 30 °C. The samples were adsorbed on chemically modified mica surface equilibrated at the same temperatures as the samples.

Atomic Force Microscopy. Reference experiments on REFE and REFH and investigations of SASE equilibrated at 15 and 30 °C and SASH equilibrated at 15 and 30 °C were performed in dry state with an AFM instrument Multimode (Digital Instruments, Santa Barbara, CA). The Multimode was operated with amplitude feedback and in a "light" tapping mode configuration. The amplitude set point was set to the maximum possible value. Silicon tips with a spring constant of 0.3 N/m and a resonance frequency of 250−300 kHz were used after calibration with gold nanoparticles (of diameter 5.22 nm) to evaluate the tip radius. The tips with radius 14.9 ± 1.9 nm were used for most measurements.

For quantitative analysis of the AFM images, the WSxM 4.0 software package,[33] MATLAB and OriginPro were used, as specified. Major emphasis was put to prove that we have been able to image single molecules. We have established histograms for volume and radius of gyration, for both samples at the equilibration temperature of 30 °C. Clusters could unambiguously be identified in the "unflattened" scan as they were significantly larger than single molecular species. Those clusters did not enter the statistical analysis. Both histograms were based on 100 individual molecules respectively. This number provides a statistically representative survey of the population of adsorbed molecules. If preferential adsorption of any size species can be excluded, this population also reflects the true molecular weight distribution of the respective sample in solution. Volume histograms were generated using the built in "flooding" parameter of WSxM 4.0 software for each molecule individually. This parameter allows the selection of a minimum threshold height in close agreement with mica surface roughness and evaluates the volume of the structure above the threshold. Similar methods have already been used for size analysis of structures on AFM images.[34,35] Radius of gyration histograms were then generated using ASCII data from AFM images and evaluating eq 6 for each molecule individually. The same thresholding method was used as applied for the volume histograms.

$$R_g^2(X, Y, Z) = \langle X^2 \rangle + \langle Y^2 \rangle - \langle X \rangle^2 - \langle Y \rangle^2 \qquad (6)$$

where

$$\langle X^2 \rangle = \sum_i X_i^2 Z_i / \sum_i Z_i \quad \text{and} \quad \langle X \rangle = \sum_i X_i Z_i / \sum_i Z_i$$

$$\langle Y^2 \rangle = \sum_i Y_i^2 Z_i / \sum_i Z_i \quad \text{and} \quad \langle Y \rangle = \sum_i Y_i Z_i / \sum_i Z_i$$

Note that the raw image produced by the AFM is an array of values $V_z(V_x, V_y)$ where V denote voltages applied to the piezos responsible for motion in the X, Y, and Z directions. The generation of ASCII data, $Z(X,Y)$ from the raw AFM image, $V_z(V_x, V_y)$ usually creates an error of ±3% for either of X, Y or Z axes, assuming that the piezos are well calibrated.[36] X_i, Y_i, and Z_i in the relations cited above are the ith piezo displacement values of X, Y, and Z respectively obtained after selection of the threshold. It must also be mentioned that the sample height may not be necessarily equal to the Z piezo displacement. This happens because the force experienced by the tip varies non linearly with tip−sample distance. Since the amplitudes involved in the "light" tapping mode configuration are rather large, complicated force vs tip−sample separation curves may result. An error analysis for this phenomenon may require numerical solutions and is way beyond the scope of this paper. The volume and radius of gyration histograms gave us concluding evidence that we have not crossed the precipitation threshold at 30 °C for either of the samples.

Results: Scattering Experiments

As has been outlined in the Experimental Section, two samples, SASE and SASH, have been identified as suitable samples for

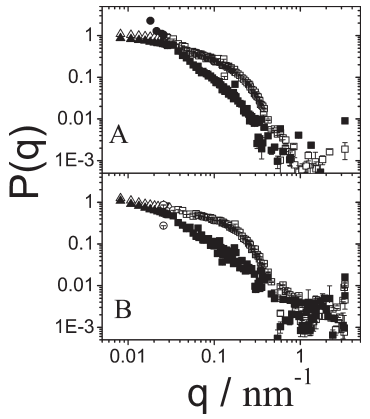

Figure 4. Scattering data of SASE (A) and SASH (B). The open symbols refer to the experiments at 30 °C, the closed symbols to the experiments at 15 °C. The triangles represent the light scattering data, the squares represent the SANS data. SANS data at $q \leq 0.025$ nm^{-1} were not utilized for any data evaluation due to their closeness to the beamstop.

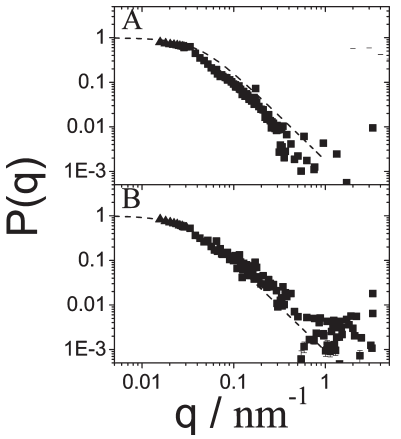

Figure 5. Scattering data of SASE (A) and SASH (B) at 15 °C as indicated in Figure 4. The dashed line is the form factor of a polydisperse ($z = 2.5$) Gaussian coil[37,38] with R_g^2 from Table 1.

SANS experiments. Both samples were generated with the sample NaPA denoted P804. With its molar mass a value of the unperturbed dimensions can be estimated to $R_g(\theta) = 41.7$ nm.[23] Taking this value as a reference, it can be seen from Table 1 that the radius of gyration of SASE at 15 °C ($R_g \approx 36$ nm) is 13% smaller than $R_g(\theta)$, whereas the $R_g = 52.8$ nm of SASH exceeds the unperturbed dimensions by more than 25%. However, both samples revealed already a considerable shrinking if compared to $R_g = 125.8$ nm measured in the absence of Ca^{2+} ions. Increasing the temperature from 15 to 30 °C causes a further coil shrinking. For SASE, $R_g \approx 25$ nm falls below the unperturbed dimensions as does $R_g = 32.8$ nm for SASH.

To obtain further information about the impact of temperature on the internal structure of the collapsing NaPA coils, SANS experiments were performed at 15 and 30 °C on both samples. The SANS data are shown together with the LS data in Figure 4. The SANS data were adjusted onto the LS data by appropriate shift factors. SANS data at $q \leq 0.025$ nm^{-1} were considered neither for this shifting nor for any further data evaluation. Due to their closeness to the beamstop those points deviate from the scattering curves without any specific trend.

At 15 °C the scattering curves of SASE and SASH show a decrease close to q^{-2} for a momentum transfer of $q \geq 0.1$ nm^{-1} indicating a coil-like structure. A comparison of the scattering curves with the Debye model curve for polydisperse coils[37,38] further supports this structure. However, as is shown in Figure 5 sample SASH is performing slightly poorer in this comparison than sample SASE does. The polydispersity is taken into account using a Schulz−Zimm distribution. The width of the distribution is described by the polydispersity parameter $z = (M_w/M_n - 1)^{-1}$, where M_w and M_n are the weight and number averaged molar masses, respectively. A value of $z = 2.5$ has been estimated from our DLS analysis.[39]

At 30 °C the scattering intensity for both samples in the same regime of momentum transfer of $q \geq 0.1$ nm^{-1} is much stronger than it is at 15 °C. At $q \geq 0.2$ nm^{-1} also a power law with an exponent close to a value of −4 appears at 30 °C. This is typical for compact particles (cf. Figure 4). Assuming that spherical subdomains may occur as structural features, we fitted both scattering curves in the regime of 0.1 nm$^{-1} \leq q \leq 0.5$ nm^{-1} with the shifted form factor of a polydisperse sphere. The sphere radius R_p and the shift factor S were fit parameters. Polydispersity was taken into account by a Schulz−Zimm distribution with a polydispersity parameter $z = 1$. For SASE and SASH sphere radii of 10.7 and 10.2 nm were established from the fit, respectively.

Another characteristic feature of the scattering curves at 30 °C is a shoulder around 0.03 nm$^{-1} \leq q \leq 0.04$ nm^{-1}. The shoulder is more pronounced for sample SASE. As was shown with molecular dynamics (MD) simulations by Limbach and Holm,[9] such a shoulder occurs in the scattering curves of pearl necklace shaped intermediates and reflects the distance between neighboring pearls. Pearl necklace shaped intermediates were suggested by Rubinstein et al.[7] as a result from the balance of the electrostatic repulsion between pearls and the surface energy of pearls in the collapsing chain. In this case the shape is that of a fully stretched pearl necklace chain. Pearl necklace shaped structures were also predicted for the intermediates of collapsing neutral chains.[5] In the latter case, the shape is close to a freely jointed chain of strings with the beads sitting on the ankles connecting neighboring strings. Neither beads nor strings are expected to be monodisperse in size.

However, quantitative model fits with such a model would require a large number of parameters. In the case of a stretched necklace, we have as a parameter the size of the beads, the number of beads, the size of the strings and the mass ratio of the string to the bead. In the case of a collapsing neutral chain, denoted as freely jointed necklace (FJN), we have in addition to consider the polydispersity of the beads and the polydispersity of the strings. In both cases, quantitative model fits also would have to take into account a considerable degree of polydispersity of the polymer mass, leading to a variation of the pearl number, a certain degree of irregularity of the shape of the beads, which do not necessarily correspond to regular spheres and finally a certain degree of flexibility of the interconnecting strings. In the light of this complex situation we decided to approach the experimental curves with two simplified features typical for necklace-like structures: (i) the sphere as a model for compact solid-like subdomains and (ii) a pair of spheres separated by a rod-like string as a model for neighboring solid subdomains, separated by linear chain segments. We utilized the model form factor of a regular FJN for further data interpretation.[40] This model is based on a freely jointed chain of monodisperse rods with compact, monodisperse spheres at the junctions and thus includes both features. In order to establish a starting point for a fit, the location of the first correlation minimum of two neighboring pearls can be used.[40] A look onto the model calculations of ref 40. suggests a crude regime of 50 nm < A < 150 nm for such a pearl−pearl distance A in our samples. This distance is fairly large and excludes FJN ensembles with a considerable fraction of species with pearl numbers N larger than 3 because this would result in overall dimensions not compatible with the respective value of R_g (Table 1). Thus, we tried to keep the model fits as simple as possible.

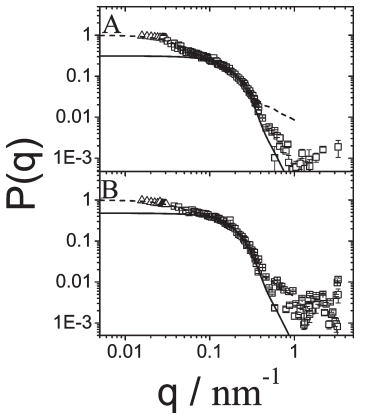

Figure 6. Data for SASE (A) and SASH (B) at 30 °C as indicated in Figure 4. Part A: (—) Form factor of a polydisperse sphere with a radius of R_p = 10.7 nm extracted from a fit in the regime of 0.1 $nm^{-1} \leq q \leq$ 0.5 nm^{-1}; (– – –) form factor of a dumbbell with a pearl radius of R_p = 10.7 nm and a distance A = 78.5 nm between the center of the pearls. Part B: (—) form factor of a polydisperse sphere with a radius of R_p = 10.2 nm extracted from a fit in the regime of 0.1 $nm^{-1} \leq q \leq$ 0.5 nm^{-1}; (– – –) sum of the form factors of a dumbbell and a polydisperse sphere with a pearl radius of R_P = 10.2 nm and a distance A = 82.0 nm between the center of the pearls. Further details are summarized in Table 2.

The scattering data of sample SASE at 30 °C were fitted with a fixed number of pearls N = 2 corresponding to a dumbbell. A fixed pearl radius R_p = 10.7 nm was adopted from the above-mentioned fit with a polydisperse sphere to the subsection of the respective scattering curve in the q-regime of 0.02 $nm^{-1} \leq q \leq$ 0.5 nm^{-1}. The number of rods is $N - 1 = 1$. The fitting parameters are the distance A between neighboring pearl centers and the ratio of the mass of one pearl m_P to the mass of one interconnecting rod m_R. As is shown in Figure 6, the fit leads to a satisfactory description of the scattering data of SASE at 30 °C for $q \leq$ 0.3 nm^{-1} with A close to 80 nm.

The same model of a dumbbell was also applied to the scattering data of sample SASH at 30 °C. Consistent with the aforementioned fit of a polydisperse sphere in the regime of 0.1 $nm^{-1} \leq q \leq$ 0.5 nm^{-1} the value for the pearl size now had to be fixed at R_P = 10.2 nm. Unfortunately, the shoulder in the case of sample SASH at 30 °C is less pronouced and no satisfactory fit could be achieved in this case with a dumbbell. As has been outlined earlier[9,14] a composition of structurally varying species could be responsible for such a blurring of the shoulder. The most simple case for a structural inhomogenity is a mixture of a dumbbell and a sphere. Therefore, we fitted the scattering data of sample SASH at 30 °C with the sum of the form factor of a dumbbell and the form factor of a polydisperse sphere. In addition to the fitting parameters A, m_R and m_P also used for sample SASE at 30 °C, we introduced the fraction w_{PS} of the polydisperse sphere as fitting parameter for sample SASH at 30 °C, leaving the fraction of the dumbbell at $1 - w_{PS}$. A common radius of 10.2 nm has been fixed for both, the z-averaged sphere radius of the polydisperse sphere fraction as well as for the pearl radius of the dumbbell component. The results of these fits are summarized in Figure 6 and Table 2. Compared to the fit with a pure dumbbell (not shown in Figure 6) addition of a fraction of polydisperse spheres considerably improves description of the scattering data for sample SASH at 30 °C.

A Kratky representation of the scattering curves $q^2P(q)$ versus q shows a characteristic maximum typical for compact structures. Therefore such a plot is highly suitable to further emphasize the charactaristics of our system at 30 °C. Figure 7 shows the Kratky representation of the scattering data at 30 °C. According to Dobrynin et al.[11] the maximum can be attributed to the pearl size

Table 2. Details of the Form Factors from the Fitting Procedure[a]

	A/nm	R_P/nm	m_P/m_R	w_{PS}	R_g/nm
SASE	78.5	10.7	0.76/1.00		31.9
SASH	82.0	10.2	0.94/1.00	0.31	28.3

[a] R_P is the pearl radius, A is the distance between the centres of the pearls, m_P/m_R is the ratio of the mass of one pearl, m_P, to the mass of one rod, m_R, connecting the pearls, and w_{PS} is the fraction of the form factor of a polydisperse sphere in the case of SASH. The last row gives the radius of gyration of the fitted model curves.

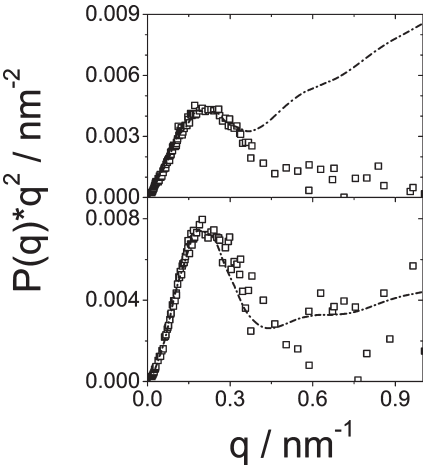

Figure 7. Data for SASE (A) and SASH (B) at 30 °C as indicated in Figure 4. The dashed lines correspond to the model form factors also represented as dashed lines in Figure 6. Details of the model parameters are summarized in Table 2.

via $R_P = 2.5/q_{max}$. As the maxima are located around 0.2 $nm^{-1} \leq q \leq$ 0.25 nm^{-1} the pearl size is between 10 and 12.5 nm which is in full agreement with the fits based on a polydisperse sphere in the regime of 0.1 $nm^{-1} \leq q \leq$ 0.5 nm^{-1}. Deviations of the theoretical dumbbell curve from experiments above q = 0.3 nm^{-1} can easily be attributed to a breakdown of the model applied by us. The rod-like strings may become completely inadequate at $q >$ 0.3 nm^{-1} if coil-like or worm-like strings interconnect neighboring pearls. Irregularities in the shape of the compact substructures, which are modeled as regular spheres may lead to further deviations in the regime of $q >$ 0.3 nm^{-1}.

Thus, a good description of the experiments at 30 °C could be achieved by the motive of a dumbbell or by a mixture of the dumbbell and a polydisperse sphere. Single spheres and/or spheres from dumbbells govern the scattering pattern in the regime of 0.07 $nm^{-1} \leq q \leq$ 0.3 nm^{-1}, which is characteristic for compact (sub)structures with a size of $R_P \approx$ 10 nm. For the spheres in the dumbbells or in the dumbbell fraction, a monodisperse sphere had been adopted. Only for the fraction of isolated spheres which coexist with dumbbells (SASH) a polydisperse sphere has been assumed. At this point we have to stress that the assumption of a polydisperse sphere contribution is inconsistent in the case of the stretched necklace strictly obeying the physics of the Rayleigh instability.[7,8,11] However, the compact substructures may not be regularly shaped spheres and the collapse may not proceed according to the Rayleigh instability. The process may rather lead to bead-like nuclei formed with variable size along a random coil in close analogy to the collapse of neutral coils.[5] This would offer various sources of polydispersities and irregularities. The motive of a dumbbell became necessary to further interpret the first shoulder occurring in between 0.03 $nm^{-1} \leq q \leq$ 0.04 nm^{-1} of the experimental curves at 30 °C. This pattern indicates that the pearls with $R_P \approx$ 10 nm are separated by a long string with $A \approx$ 80 nm in full agreement with an earlier experiment on the same system.[14] The

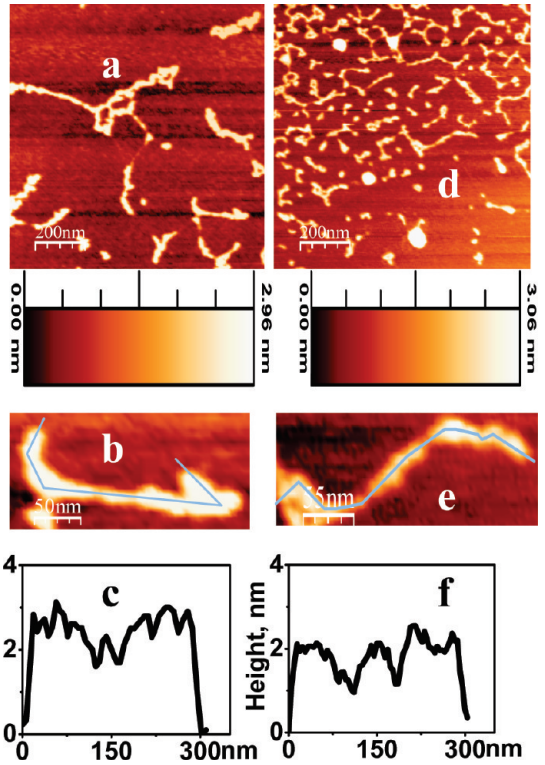

Figure 8. Reference samples REFE and REFH measured at room temperature. The reference samples are free of $CaCl_2$ but have the same NaPA concentrations as sample SASE and SASH respectively, presented in Figures 9−13 with c = 0.2346 g/L (REFE) and c = 0.1300 g/L (REFH) and [NaCl] = 10.00 mM. In either case, polyacrylates do not show any significant collapsed subdomains. Key: (a) AFM topography image for REFE; (b) zoom of the image a; (c) height profile taken along a single chain as shown by the line in the zoom image b; (d) AFM topography image for REFH; (e) zoom of the image d; (f) height profile taken along a single chain as shown by the line in the zoom image e.

interpretation just presented most likely is not exclusive. Mixtures of pearl necklaces with various numbers of pearls in the regime of $1 \leq N \leq 3$ could also satisfactorily reproduce our data. Only fits with pearl number $N \geq 4$ did not lead to satisfactory fits anymore. With $N \geq 4$ and a fixed pearl−pearl separation of A ≈ 80 nm, we also could not keep the overall size as low as our values from light scattering suggested (Table 1). Several alternative models without the feature of a pearl necklace were also tested with the data of SASE at 30 °C but either failed or had to be discarded for physical reason (details of this discussion are presented in the Supporting Information). Therefore, the system of a simple dumbbell (SASE) or of a mixture of a dumbbell with a polydisperse sphere (SASH) are considered to correctly depict the average features of possibly more complex real systems. With these facts in mind, the results indicate intermediates with a very small number of $1 \leq N \leq 3$ of pearls per chain.

Finally, we will address the enhancement of the shrinking observed for the CaPA system with increasing temperature. The shrinking process comprises two steps. First, Ca^{2+} binds to COO^- residues, in an entropy driven liberation of 10 water molecules and 2 Na^+ ions per bound Ca^{2+} ion.[21] This corresponds to a chemical modification of the chain, which gets less polar and therefore less soluble in water. As a consequence, the neutralizing coil collapses in a second step. According to our findings, the collapse seems to bear more similarities with the collapse of a neutral coil in a poor solvent than with the model of a stretched pearl necklace subdued to a Rayleigh-instability. The latter is supported by the observation that the intermediates observed at 15 °C have already adopted a coil-like structure.

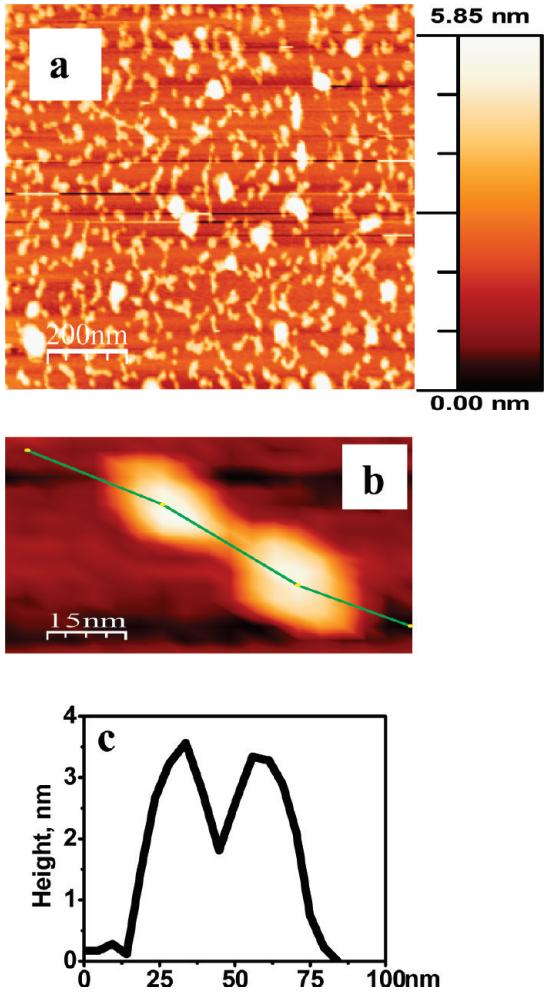

Figure 9. Adsorption of sample SASE equilibrated at 15 °C onto freshly cleaved mica, treated with a solution of 0.01 g/L $LaCl_3$. Presence of Ca^{2+} ions drastically reduces the size of coils and sections within the chain begin to collapse into subdomains. Key: (a) AFM topography image; (b) zoom of the image a showing a well resolved single molecule; (c) height profile taken along a single chain as shown by the line in the zoom image b.

If this coil further collapses, pearls form along a random coil rather than along a straight line.

Results: AFM Experiments

The two samples SASE and SASH analyzed with SANS were also investigated by AFM experiments. In this section, we focus on AFM experiments. We begin with a description of the two reference samples, which are the Ca^{2+} free analogues of SASE and SASH.

Parts a−c and parts d−f of Figure 8 show exemplary AFM scans for REFE and REFH, respectively, along with their height profiles. The images show extended configurations of NaPA chains. Further resolution of these structures to a statistically significant amount of isolated single molecules was not possible. It was observed that adsorption of the negatively charged polyacrylate coils on negative mica surfaces was weak. We suspect that even after treating mica surfaces with 0.01 g/L $LaCl_3$ solution, the surface is still slightly undercharged and prevents strong trapping of the reference samples. However, a visual comparison of these images with those of SASE and SASH shown in Figures 9−12 clearly reveals a much greater extension for the chains without Ca^{2+} ions than the same chains show in the presence of Ca^{2+} ions.

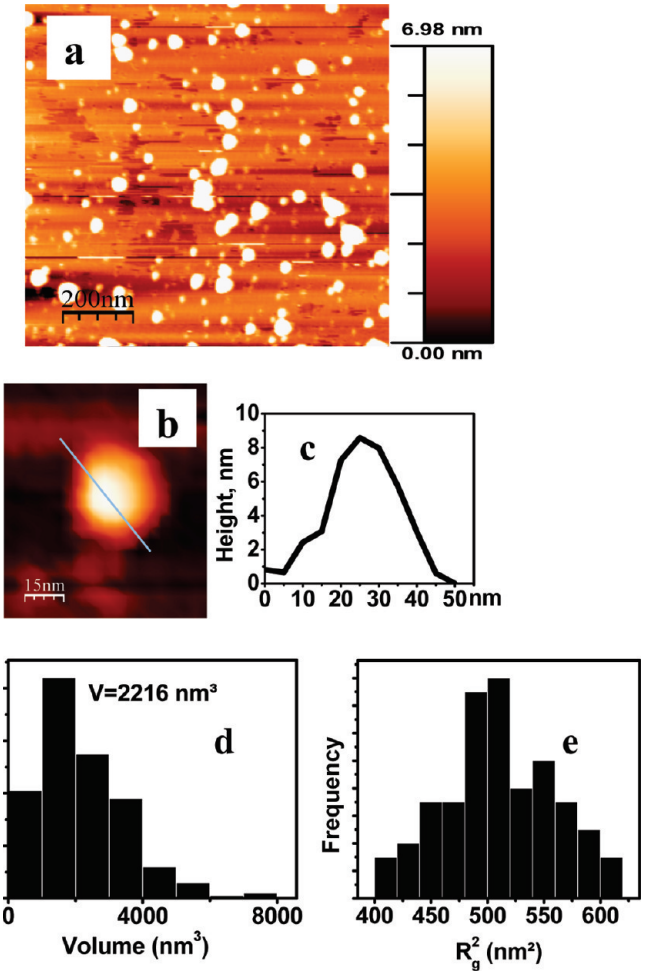

Figure 10. Adsorption of sample SASE equilibrated at 30 °C onto freshly cleaved mica, treated with a solution of 0.01 g/L $LaCl_3$. The shrinking effect caused by Ca^{2+} ions is much more pronounced compared to the effect observed after equilibration at 15 °C (Figure 9). Key: (a) AFM topography image; (b) zoom of the image a showing a well resolved collapsed single molecule; (c) height profile taken across the collapsed structure as shown by the line in the zoom image b; (d) volume histogram (for original scan, not deconvoluted to account for geometry of the tip) showing a mean volume of 2216 nm^3; (e) the mean squared radius of gyration histogram, showing a mean of R_g^2 = 510.8 nm^2.

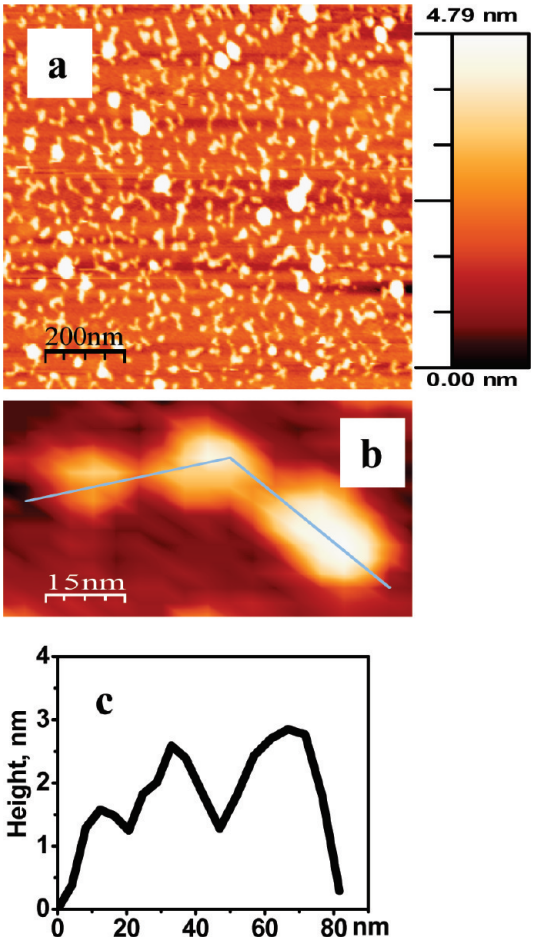

Figure 11. Adsorption of sample SASH equilibrated at 15 °C onto freshly cleaved mica, treated with a solution of 0.01 g/L $LaCl_3$. Presence of Ca^{2+} ions drastically reduces the size of coils and sections within the chain begin to collapse into subdomains. Key: (a) AFM topography image; (b) zoom of the image a showing a well resolved single molecule; (c) height profile taken along a single chain as shown by the line in the zoom image b.

A closer inspection of Figures 9−12 reveals further details. Parts a−c of Figure 9 show an exemplary AFM scan for SASE equilibrated at 15 °C along with the height profile of a well resolved single molecule. Parts a−e of Figure 10 show an exemplary AFM scan for SASE equilibrated at 30 °C along with the height profile of a well resolved collapsed single molecule and with histograms for volumes and mean squared radii of gyration. At the higher equilibration temperature, the collapse shown by a polyacrylate coil is much more pronounced. The same trend is observed for SASH as the equilibration temperature goes from 15 to 30 °C. Parts a−c of Figure 11 show an exemplary AFM scan for SASH equilibrated at 15 °C along with the height profile of a well resolved single molecule. Parts a−e of Figure 12 show an exemplary AFM scan for SASH equilibrated at 30 °C along with the height profile of a well resolved collapsed single molecule and with histograms for volumes and mean squared radii of gyration.

An inevitable effect during AFM imaging of structures showing dense pattern of collapsed subdomains is that it is extremely difficult to probe vertical features.[41] The well-known tip broadening effect further accentuates the situation. Nevertheless, AFM was able to identify rarely occurring clusters: AFM scans at the equilibrium temperature of 15 °C (Figure 9a for SASE and Figure 11a for SASH) show small globules and some large clusters of polyacrylate chains in addition to partially collapsed polyacrylate coils. A few clusters also occur at the equilibrium temperature of 30 °C (Figure 10a for SASE and Figure 12a for SASH). It is believed that flux drying of surfaces, and the resulting capillary forces, may cause compaction of some coils into globules especially in the case of weak adsorption of polyelectrolytes.[18] This compaction further deteriorates the quality of adsorption on the surface and promotes coalescence of globules to clusters.

Quantitative analysis was not performed at the equilibration temperature of 15 °C largely because we were unsure whether in some cases the globules represent single molecules or sections of an extended coil which may partly remain invisible to a scan considering the noise levels at which AFM experiments were performed.[18] Thus, only AFM scans produced at equilibration temperature of 30 °C were quantitatively analyzed. Analysis was based on sets of particles identified as single polymers, which included shapes like globules, sausage-like structures and dumbbells, resulting in a volume histogram for SASE and SASH respectively, equilibrated at 30 °C. Assuming the dry state density of the NaPA−Ca^{2+} system to be 1 g/cm^3, we can approximate the volume of a molecule with a molecular weight of 783 000 g/mol to be 1685 nm^3. The mean volumes shown by our histograms are only insignificantly higher.

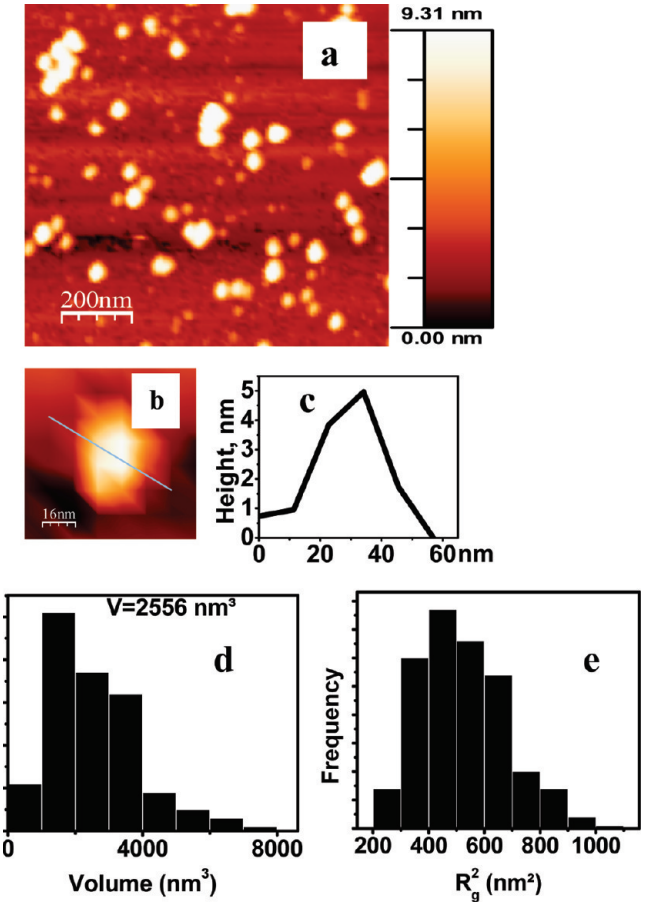

Figure 12. Adsorption of sample SASH equilibrated at 30 °C onto freshly cleaved mica, treated with a solution of 0.01 g/L $LaCl_3$. The shrinking effect caused by Ca^{2+} ions is much more pronounced compared to the effect observed after equilibration at 15 °C (Figure 11). Key: (a) AFM topography image; (b) zoom of the image a showing a well resolved collapsed single molecule; (c) height profile taken across the collapsed structure as shown by the line in the zoom image b; (d) volume histogram (for original scan, not deconvoluted to account for geometry of the tip) showing a mean volume of 2556 nm^3; (e) the mean squared radius of gyration histogram, showing a mean of R_g^2 = 523.0 nm^2.

Deconvolution to account for geometry of the tip would bring the numbers still closer to theoretical approximations. Hence, the volume histograms give concluding evidence that we have been able to predominantly visualize isolated single molecules.

In line with R_g from SLS, we estimated root mean squares of the z-averaged squared radius of gyration for SASE and SASH at the equilibration temperature of 30 °C according to

$$R_g^2(\mathrm{AFM}) = \frac{\sum_{i=1}^{100} V_i^2 R_{gi}^2}{\sum_{i=1}^{100} V_i^2} \qquad (7)$$

where the sums in eq 7 include all individual molecules i. A comparison of R_g values obtained for SASE and SASH at the equilibration temperatures of 30 °C from light scattering and AFM is given in Table 3. For both samples, R_g(AFM) gets close to R_g(SLS). Once more, this indicates that AFM predominantly captured well separated polymers at 30 °C. Remaining discrepancies may be attributed to capillary forces during flux drying which tend to shrink the chains.

Table 3. Number Averaged Volumes and Radii of Gyration R_g(AFM) Calculated from AFM (Eq 7) and R_g(SLS) from Light Scattering (Eq 1) at the Equilibration Temperature of 30 °C

sample	[PA]/ (mmol/L)	[Ca^{2+}]/ (mmol/L)	volume/nm^3	R_g(AFM)/nm	R_g(SLS)/nm
SASE-30 °C	2.50	1.00	2216	22.60	25.6 ± 1.0
SASH-30 °C	1.38	0.65	2556	22.87	32.8 ± 1.6

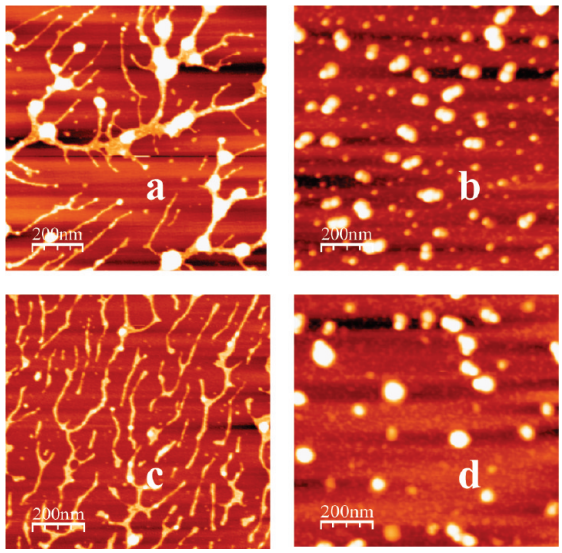

Figure 13. Adsorption of Ca−PA onto mica surface chemically modified using APDMES: (a) SASE equilibrated at 15 °C; (b) SASE equilibrated at 30 °C; (c) SASH equilibrated at 15 °C; (d) SASH equilibrated at 30 °C. Samples equilibrated at 30 °C are considerably more collapsed than the samples equilibrated at 15 °C.

More important, we note the following qualitative picture: once the conformation in solution reaches a random coil state (equilibration temperature of 15 °C), the conformation on surface already begins to show signs of pearl formation. When the conformation in solution shows a pearl-necklace-like structure (equilibration temperature of 30 °C), the conformation on surface is that of a tightly packed globule, sausage-like structure or a dumbbell. Although the substrate-sample interactions are not very clearly understood,[27,28,42−44] they seem to play an important role in our case. The present results, generated for polyacrylates with Ca^{2+} cations, add information to systems with weak adsorption forces and mark a departure from similar studies[17,45] made earlier when adsorption forces were rather strong.

This temperature induced collapse of the PA-Ca^{2+} system was also imaged using mica surface chemically modified with APDMES. Parts a−d of Figure 13 show exemplary AFM scans for SASE (15 °C), SASE (30 °C), SASH (15 °C) and SASH (30 °C), respectively, as adsorbed on chemically modified mica. Again, partially collapsed NaPA−Ca^{2+} chains further collapse with increase of equilibration temperature. However, shear fields created during drying procedures have a profound impact on the molecules adsorbed on modified mica surfaces after being equilibrated at 15 °C. At the equilibration temperature of 30 °C, the results on chemically modified mica surfaces are similar to ones on $LaCl_3$ treated substrates with the difference that no large clusters are seen, indicating that chemical modification inhibits clustering.

It is relevant here to mention that the structure of the adsorbed coils visualized by AFM does not exactly reproduce the structure in solution. Yet, AFM experiments clearly reproduce the Ca^{2+}

and temperature induced collapse observed by scattering experiments in solution at least qualitatively. AFM thus provides interesting information on adsorbed Na−PA−Ca^{2+} chains supplementary to the scattering data on the respective dilute solution behavior.

Summary

Addition of alkaline earth cations to dilute solutions of long chain NaPA in 0.01 M NaCl induces a coil collapse of the extended polyelectrolyte chains. The presence of such specifically interacting cations also introduces a new sensitivity of chain morphology toward temperature which is not detectable if the NaPA coils are just dissolved in aqueous 0.01 M NaCl.

This characteristic response of anionic NaPA coils was successfully used in the present contribution to induce a coil-to-globule collapse with a cascade of intermediates. The main goal was to investigate the shape of these intermediates. Such intermediates were investigated for the first time by applying LS, SANS and AFM to the same samples. SANS experiments on two different samples with similar concentrations of the components provided clear evidence that an increase of the temperature from 15 to 30 °C transformed a partially collapsed coil into a necklace-like shape. The pearl necklace feature was identified by two characteristic shoulders in the low q-regime of the scattering curve and a successive q^{-4} decay. Whereas the first aspect indicates a nearest neighbor correlation of pearls separated by a characteristic distance A, the second aspect proves the existence of smooth phase boundaries between the scattering objects and the medium which supports the existence of compact pearl-like subdomains.

The scattering data of the two intermediates captured at 30 °C could be described by either a dumbbell or a mixture of a dumbbell and a sphere. The resulting numbers of pearls per polymer are considered to be only average values of the actual distributions of the number N of beads per polymer. The resulting average values of $N = 2$ and $1 < N < 2$ observed for the two samples indicate a distribution of a very low number of beads per polymer for the present system at 30 °C. A larger number of beads per polymer led to unacceptably large overall dimensions because the bead−bead distance had to be fixed to 80 nm. The impact of this large bead−bead separation on polymer size is even larger in the case of a stretched necklace than in the case of a freely jointed necklace. Thus, the latter shape is more likely to occur with the species with $N \geq 2$ for the present system. This is even more so as the shape has already adopted a random coil-like structur at 15 °C due to electrostatic screening by the added NaCl.

AFM experiments performed with the same samples also showed reproducible differences between the NaPA coils with and without Ca^{2+} cations and between the state of the coils equilibrated at 15 and 30 °C respectively. These differences run parallel with the coil transformations observed with scattering results. The drastic increase of the degree of collapse on increasing the temperature could be recovered with AFM experiments by simply equilibrating the solutions prior to adsorption on equilibrated substrates. However, as the adsorption process preceding AFM imaging enhances the tendency of the coils to collapse, the structures revealed by AFM are not identical to the corresponding shapes observed by scattering in solution in the present system.

Joint scattering and AFM experiments revealed reproducible changes of polyelectrolyte structure induced by subtle changes of Ca^{2+} concentrations and temperature. These findings are expected to be of special relevance for the development of materials responsive to different solvent conditions.

Acknowledgment. Financial support of the Deutsche Forschungsgemeinschaft (grant HU807/7 of Paderborn group and STA324/23 of Dresden group) as well as helpful discussion with Prof. Loewen and Dr. Messina are gratefully acknowledged.

Supporting Information Available: Evaluation of data from static light scattering (SLS) and application of alternative models to describe combined SLS−SANS curves including figures and tables. This material is available free of charge via the Internet at http://pubs.acs.org.

References and Notes

(1) Stockmayer, W. H. *Makromol. Chem.* **1960**, *35*, 54–74.
(2) de Gennes, P.-G. *J. Phys. Lett.* **1975**, *36*, L55–L57.
(3) Sun, S.-T.; Nishio, I.; Swislow, G.; Tanaka, T. *J. Chem. Phys.* **1980**, *73*, 5971–5975.
(4) Chu, B.; Ying, Q.; Grosberg, Y. *Macromolecules* **1995**, *28*, 180–189.
(5) Kuznetsov, Y. A.; Timoshenko, E. G.; Dawson, K. A. *J. Chem. Phys.* **1995**, *103*, 4807–4818.
(6) Kantor, Y.; Kardar, M. *Europhys. Lett.* **1994**, *27*, 643–648.
(7) Dobrynin, A. V.; Rubinstein, M.; Obukhov, S. P. *Macromolecules* **1996**, *29*, 2974–2979.
(8) Schiessel, H. *Macromoelcules* **1999**, *32*, 5673–5680.
(9) Limbach, H. J.; Holm, C. *J. Phys. Chem. B* **2003**, *107*, 8041–8055.
(10) Uyaver, S.; Seidel, C. *J. Phys. Chem. B* **2004**, *108*, 18804–18814.
(11) Liao, Q.; Dobrynin, A. V.; Rubinstein, M. *Macromolecules* **2006**, *39*, 1920–1938.
(12) Schweins, R.; Goerigk, G.; Huber, K. *Eur. Phys. J. E* **2006**, *21*, 99–110.
(13) Aseyev, V. O.; Klenin, S. I.; Tenhu, H.; Grillo, I.; Geissler, E. *Macromolecules* **2001**, *34*, 3706–3709.
(14) Schweins, R.; Lindner, P.; Huber, K. *Macromolecules* **2003**, *36*, 9564–9573.
(15) Spiteri, M. N.; Williams, C. E.; Boué, F. *Macromolecules* **2007**, *40*, 6679–6691.
(16) Minko, S.; Kiriy, A.; Gorodyska, G.; Stamm, M. *J. Am. Chem. Soc.* **2002**, *124*, 3218–3219.
(17) Kiriy, A.; Gorodyska, G.; Minko, S.; Jaeger, W.; Stepanek, P.; Stamm, M. *J. Am. Chem. Soc.* **2002**, *124*, 13454–13462.
(18) Kirwan, L. J.; Papastavrou, G.; Borkovec, M.; Behrens, S. H. *Nano Lett.* **2004**, *4*, 149–152.
(19) Netz, R. R.; Joanny, J. -F. *Macromolecules* **1999**, *32*, 9013–9025.
(20) Schweins, R.; Huber, K. *Eur. Phys. J E* **2001**, *5*, 117–126.
(21) Sinn, C. G.; Dimova, R.; Antonietti, M. *Macromoelcules* **2004**, *37*, 3444–3450.
(22) Lages, S.; Schweins, R.; Huber, K. *J. Phys. Chem. B* **2007**, *111*, 10431–10437.
(23) Schweins, R.; Hollmann, J.; Huber, K. *Polymer* **2003**, *44*, 7131–7141.
(24) Lindner, P. In *Neutrons, X-rays and Light: Scattering methods applied to soft condensed matter*; Lindner P., Zemb, Th., Eds.; Elsevier: Amsterdam, 2002, Part I, Chapter 2
(25) Lindner, P. *J. Appl. Crystallogr.* **2000**, *33*, 807–811.
(26) Kumaki, J.; Hashimoto, T. *J. Am. Chem. Soc.* **2003**, *125*, 4907–4917.
(27) Berg, J. M.; Claesson, P. M.; Neuman, R. D. *J. Colloid Interface Sci.* **1993**, *161*, 182–189.
(28) Abraham, T.; Kumpulainen, A.; Xu, Z.; Rutland, M.; Claesson, P. M.; Masliyah, J. *Langmuir* **2001**, *17*, 8321–8327.
(29) Bustamante, C.; Vesenka, J.; Tang, C. L.; Rees, W.; Guthold, M.; Keller, R. *Biochemistry* **1992**, *31*, 22–26.
(30) Vesenka, J.; Guthold, M.; Tang, C. L.; Keller, D.; Delaine, E.; Bustamante, C. *Ultramicroscopy* **1992**, *42−44*, 1243–1249.
(31) You, H. X.; Lowe, C. R. *J. Colloid Interface Sci.* **1996**, *182*, 586–601.
(32) Bezanilla, M.; Manne, S.; Laney, D. E.; Lyubchenko, Y. L.; Hansma, H. G. *Langmuir* **1995**, *11*, 655.
(33) I. Horcas et al. *Rev. Sci. Instrum.* **2007**, *78*, 013705-013705-8
(34) Gorodyska, G.; Kiriy, A.; Minko, S.; Tsitsilianis, C.; Stamm, M. *Nano Lett.* **2003**, *3*, 365–368.
(35) Kiriy, A.; Gorodyska, G.; Minko, S.; Tsitsilianis, C.; Stamm, M. *Macromolecules* **2003**, *36*, 8704–8711.
(36) Digital Instruments Veeco Metrology Group, MultiMode SPM Instruction Manual, Version 4.31ce, 1997.
(37) Greschner, G. S. *Makromol. Chem.* **1973**, *170*, 203.

(38) Zimm, B. *J. Chem. Phys*. **1948**, *16*, 1099–1116.
(39) Koppel, D. E. *J. Chem. Phys*. **1972**, *57*, 4814–4820.
(40) Schweins, R.; Huber, K. *Macromol. Symp*. **2004**, *211*, 25–42.
(41) Watanabe, M.; Baba, S.; Nakata, T.; Morimoto, T.; Sekino, S. In *Metrology, Inspection and Process Control for Microlithography XXII*; Allgair, J. A., Raymond, C. J., Eds.; *Proc. SPIE* 69220J-1-14; San Jose, CA, 2008.
(42) Guldberg-Pedersen, H.; Bergström, L. *Acta Mater* **2000**, *48*, 4570.
(43) Guldberg-Pedersen, H.; Bergström, L. *J. Am. Ceram. Soc*. **1999**, *82*, 1137.
(44) Laarz, E.; Meurk, A.; Yanez, J. A.; Bergström, L. *J. Am. Ceram. Soc*. **2001**, *84*, 1675.
(45) Rivetti, C.; Guthold, M.; Bustamante, C. *J. Mol. Biol*. **1996**, *264*, 919–932.